

See discussions, stats, and author profiles for this publication at: <https://www.researchgate.net/publication/231239904>

# Wired Porous Cathode Materials: A Novel Concept for Synthesis of $\text{LiFePO}_4$

ARTICLE in CHEMISTRY OF MATERIALS · MAY 2007

Impact Factor: 8.35 · DOI: 10.1021/cm062843g

CITATIONS

153

READS

113

7 AUTHORS, INCLUDING:



Jean-Michel Goupil

National Graduate School of Engineering an...

38 PUBLICATIONS 1,074 CITATIONS

SEE PROFILE



Miran Gaberscek

National Institute of Chemistry

181 PUBLICATIONS 4,595 CITATIONS

SEE PROFILE



Darko Hanzel

Jožef Stefan Institute

83 PUBLICATIONS 1,606 CITATIONS

SEE PROFILE



Iztok Arcon

University of Nova Gorica

226 PUBLICATIONS 2,174 CITATIONS

SEE PROFILE

# Wired Porous Cathode Materials: A Novel Concept for Synthesis of $\text{LiFePO}_4$

Robert Dominko,<sup>†</sup> Marjan Bele,<sup>†</sup> Jean-Michel Goupil,<sup>‡</sup> Miran Gaberscek,<sup>\*,†</sup> Darko Hanzel,<sup>§</sup> Iztok Arcon,<sup>||</sup> and Janez Jamnik<sup>†</sup>

National Institute of Chemistry, Hajdrihova 19, SI-1000 Ljubljana, Slovenia, ENSICAEN, UMR CNRS 6506, Catalyse & Spectrochimie Lab, F-14050 Caen, France, Jozef Stefan Institute, Jamova 39, SI-1000 Ljubljana, Slovenia, and Nova Gorica Polytechnic, P.O. Box 301, 5001, Nova Gorica, Slovenia

Received November 30, 2006. Revised Manuscript Received February 15, 2007

To increase the power density of battery materials, without significantly affecting their main advantage of a high energy density, novel material architectures need to be developed. Using the example of  $\text{LiFePO}_4$ , we demonstrate a simple, sol–gel-based route that leads to large (up to 20  $\mu\text{m}$ ) primary  $\text{LiFePO}_4$  particles, each of which contains hierarchically organized pores in the meso and macro range. As the pores are formed due to vigorous gas evolution (mainly  $\text{CO}$  and  $\text{CO}_2$ ) during degradation of a citrate precursor, they are perfectly interconnected within each particle. Elementary carbon, the other citrate-degradation product, is deposited on the walls of emerging pores. The superposition of a continuous 1–2 nm thick carbon film (electron conductor) on pores (ion conductor when filled with electrolyte) represents a unique architecture in which the electrons and ions are simultaneously supplied to the site of insertion in the particle interior. The material can operate at current rates up to 50 C while preserving a high tap density of ca. 1.9  $\text{g cm}^{-3}$ .

## 1. Introduction

Creation of novel battery materials with advanced properties is motivated by two major driving forces: to increase the energy density or power density of a battery.<sup>1</sup> While the increase of energy density is only possible through invention of new compounds with more favorable inherent thermodynamic properties, maximization of power can be achieved by preparing various kinds of intricate electrode architectures that typically consist of at least three intertwined phases. Each of these phases possesses a different functionality: in the active bulk compound the charge is stored, whereas the other two phases, each with the form of a 3-D web, serve for fast ionic and electronic transport to/from the active compound. Examples of the latter two phases are liquid electrolyte and carbon black particles, respectively.<sup>2</sup> With the discovery of high energy density but low-conductivity active compounds (especially olivines with room-temperature conductivity  $<10^{-9} \text{ Scm}^{-1}$ ),<sup>3</sup> even more advanced techniques had to be developed. While preserving the 3-D interconnectivity of both conductive phases, these advanced techniques introduced fine nanoscale structuring of all three phases (typically in the range of 10–100 nm).<sup>4–10</sup> Using such nanostructuring, Nyten et al.,<sup>11</sup> as well as our laboratory,<sup>12</sup> recently demon-

strated that a remarkable activity can even be imparted to the class of silicates, i.e., materials that have been traditionally considered perfect insulators. On the other hand, when appropriate nanostructuring is used with moderately or even highly conductive active compounds, exceptionally high power densities can be achieved. Two good recent examples are  $\text{LiFePO}_4$  nanofibers decorated with carbon nanoparticles<sup>13</sup> that gave considerable capacities at current densities as high as 60 C and the high surface area, nanowire-based  $\text{LiCoO}_2$  material prepared via a hard templating route<sup>14</sup> that showed a significantly improved rate performance if compared to the standard material. The crucial common features that in those and similar cases<sup>15–17</sup> allow such extreme current (or power) densities is the openness of the basic materials

\* To whom correspondence should be addressed. E-mail: miran.gaberscek@ki.si

<sup>†</sup> National Institute of Chemistry.

<sup>‡</sup> ENSICAEN.

<sup>§</sup> Jozef Stefan Institute.

<sup>||</sup> Nova Gorica Polytechnic.

(1) Tarascon, J.-M.; Armand, M. *Nature* **2001**, *414*, 359.

(2) (a) Dominko, R.; Gaberscek, M.; Drofenik, J.; Bele, M.; Jamnik, J. *Electrochim. Acta* **2003**, *48*, 3709. (b) Dominko, R.; Gaberscek, M.; Drofenik, J.; Bele, M.; Jamnik, J. *J. Power Sources* **2003**, *119*, 770.

(3) Padhi, A. K.; Nanjundaswamy, K. S.; Goodenough, J. B. *J. Electrochem. Soc.* **1997**, *144*, 1188.

(4) Garcia-Moreno, O.; Alvarez-Vega, M.; Garcia-Alvarado, F.; Garcia-Jaca, J.; Gallardo-Amores, J. M.; Sanjuan, M. L.; Amador, U. *Chem. Mater.* **2001**, *13*, 1570.

(5) Ravet, N.; Goodenough, J. B.; Besner, S.; Simoneau, M.; Hovington, P.; Armand, M. In *Proceedings of the 196th ECS Meeting*, Hawaii, Oct 1999; The Electrochemical Society: Pennington, NJ; pp 17–22.

(6) Huang, H.; Yin, S. C.; Nazar, L. F. *Electrochem. Solid-State Lett.* **2001**, *4*, A170.

(7) Chen, Z. H.; Dahn, J. R. *J. Electrochem. Soc.* **2002**, *149*, A1184.

(8) Herle, P. S.; Ellis, B.; Coombs, N.; Nazar, L. F. *Nat. Mater.* **2004**, *3*, 147.

(9) Dominko, R.; Bele, M.; Gaberscek, M.; Remskar, M.; Hanzel, D.; Pejovnik, S.; Jamnik, J. *J. Electrochem. Soc.* **2005**, *152*, A607.

(10) Dominko, R.; Goupil, J. M.; Bele, M.; Gaberscek, M.; Remskar, M.; Hanzel, D.; Jamnik, J. *J. Electrochem. Soc.* **2005**, *152*, A858.

(11) Nyten, A.; Abouimrane, A.; Armand, M.; Gustafsson, T.; Thomas, J. O. *Electrochem. Commun.* **2005**, *7*, 156.

(12) Dominko, R.; Bele, M.; Gaberscek, M.; Meden, A.; Remskar, M.; Jamnik, J. *Electrochem. Commun.* **2006**, *8*, 217.

(13) Sides, C. R.; Croce, F.; Young, V. Y.; Martin, C. R.; Scrosati, B. *Electrochem. Solid State* **2005**, *8*, A484.

(14) Jiao, F.; Shaju, K. M.; Bruce, P. G. *Angew. Chem., Int. Ed.* **2005**, *44*, 6550.

(15) Du Pasquier, A.; Plitz, I.; Gural, J.; Badway, F.; Amatucci, G. G. *J. Power Sources* **2004**, *136*, 160.

structure combined with very short typical distances ( $<10$  nm), along which the solid-state part of lithium transport occurs. The openness of the basic nanostructure of the active material makes the subsequent deposition of a thin electronically conducting solid phase (usually carbon) much easier, and it also facilitates access of ion-conducting liquid electrolyte to the whole surface of the active material. In this way, the active substrate is perfectly supplied with both electrons and ions. However, the limiting architectures created using this approach may bear more resemblance to supercapacitors<sup>18</sup> than to conventional insertion batteries.<sup>1</sup> In other words, while the openness of the structure may effectively solve the problem of slow charge transport, it also, by definition, negatively affects the main advantage of batteries—their high energy density.

Hence, to introduce fast ionic and electronic paths into a battery electrode, with the aim to either exploit low-conductivity materials or prepare a high-power battery, while preserving the high energy density of the starting material, new concepts of electrode structuring are needed. On examining the various effective transport systems seen in nature (river systems, water distribution in plants, the cardiovascular system) or those established artificially (webs of roads, distribution of electricity, etc.), one finds that the transport paths in all these systems are organized hierarchically: the narrowest and shortest paths merge into medium-sized paths, which in turn flow into the longest and widest “arteries”. In the present paper, we show how a similar hierarchical transport system can be created within a Li battery electrode. The core of this system is a hierarchical web of pores/apertures that forms within individual, relatively large ( $1\text{--}20\text{ }\mu\text{m}$ ) active particles during heat treatment of an initial xerogel. After being filled with liquid electrolyte during battery assembly, the pores should serve as fast ion conductors. The hierarchical nature of porous webs can be achieved through combustion of homogeneously (on the molecular level) distributed organic precursors in the initial xerogel. The evolving gases, which are the main products of organic combustion, will penetrate through the softened amorphous xerogel in the same stochastic way as observed, for example, in the flow of surface waters toward oceans—hence, the similar hierarchical pattern. Most importantly, the other product of organic combustion, i.e., solid electron-conducting carbon, will also be homogeneously distributed within the final composite material. The exact location/distribution of this carbon is also a subject of the present investigation. In any case, during battery operation this carbon film is expected to serve as a fast electronic path along which electrons are supplied into the interior of active particles.

The proposed strategy of materials structuring is demonstrated using the example of  $\text{LiFePO}_4$ , one of the most attractive and extensively researched cathode materials.<sup>1–10</sup> A previous investigation showed that combustion of suitable

organic precursors led to formation of a several nanometer thick, uniform film on the surface of  $\text{LiFePO}_4$ ,<sup>9</sup> and a moderate porosity was also detected in these samples.<sup>10</sup> However, at that point neither the mechanism of materials formation nor the precise (nano)architecture were known. The present study clearly identifies the most important structural and compositional changes during heat treatment of initial xerogels. The results of eight complementary techniques reveal the actual scenario of materials structuring. In this way, we demonstrate for the first time the role of hierarchical organization of conductive paths, both ionic and electronic, in achieving a high rate and high-density battery electrode.

## 2. Experimental Section

Several series of  $\text{LiFePO}_4/\text{C}$  composites were prepared by a sol–gel method. First,  $\text{Fe(III)}$  citrate (Aldrich, 22,897-4) was dissolved in water at  $60\text{ }^\circ\text{C}$ . Separately, an equimolar water solution of  $\text{LiH}_2\text{PO}_4$  was prepared from  $\text{H}_3\text{PO}_4$  (Merck 1.00573) and  $\text{Li}_3\text{PO}_4$  (Aldrich, 33,889-3). The solutions were mixed together, and the obtained transparent sol was dried at  $60\text{ }^\circ\text{C}$  for at least 24 h. After thorough grinding with a mortar and pestle, the obtained dried xerogel was fired in argon atmosphere for 10 h at selected temperatures. The heating rate was  $5\text{ K/min}$ . Temperatures for preparation of intermediate LFP composites were selected from a basic TGA curve. The following intermediate LFP composites were prepared: LFP155 (fired at  $155\text{ }^\circ\text{C}$  for 1 h), LFP200 (fired at  $200\text{ }^\circ\text{C}$  for 1 h), LFP310 (fired at  $310\text{ }^\circ\text{C}$  for 1 h), LFP465 (fired at  $465\text{ }^\circ\text{C}$  for 1 h), and LFP550 (fired at  $550\text{ }^\circ\text{C}$  for 1 h). For analyses, the starting xerogel (denoted as LFPgel) and the final  $\text{LiFePO}_4/\text{C}$  composite (denoted as LFP700) were also used.

Thermogravimetry analysis (TGA-DTA) was performed on a Netzsch STA 409 instrument connected to an Inficon Leybold Quadrex 200 quadropole mass spectrometer.

X-ray powder diffraction (XRD) patterns were measured on a Philips diffractometer PW 1710 using  $\text{Cu K}\alpha$  radiation in  $0.04^\circ$   $2\theta$  steps from  $10^\circ$  to  $80^\circ$ .

Infrared-attenuated total reflection (IR-ATR) spectroscopy was performed using a Perkin–Elmer 2000 spectrometer (resolution  $4\text{ cm}^{-1}$ ).

$^{57}\text{Fe}$  Mössbauer experiments were performed at room temperature using a constant acceleration spectrometer. The source was  $^{57}\text{Co}$  in a Rh matrix. Velocity calibration and isomer shifts (IS) are quoted relative to an absorber of metallic iron at room temperature. The experiments were performed in both transmission and scattering geometry. Conversion electron Mössbauer measurements in a  $\text{He}/\text{CH}_4$  gas flow proportional counter were performed in order to find differences in the depth distribution of Fe cations between the surface of the samples and the bulk. Parameter fits were performed using a standard least-squares fitting routine with Lorentzian lines.

The textural properties were studied using a FEI-SEM (Supra LV35). The properties of the porous system in the 4 to 200 nm range were determined by nitrogen adsorption at  $77\text{ K}$  using an ASAP 2000 instrument from Micromeritics. As-prepared samples of mass around 200 mg were evacuated at  $120\text{ }^\circ\text{C}$  under  $0.1\text{ Pa}$  prior adsorption.

Preparation of electrodes for electrochemical testing and settings for electrochemical testing is described elsewhere.<sup>10</sup> The constant current during cell cycling was set to a value of  $85\text{ mA/g}$  (roughly  $\text{C}/2$ ). The geometric surface area of the working electrode was always  $0.5\text{ cm}^2$ .

X-ray absorption spectra in the energy region of the Fe K edge were measured in transmission mode at E4 beamline of the

(16) Plitz, I.; DuPasquier, A.; Badway, F.; Gural, J.; Pereira, N.; Gmitter, A.; Amatucci, G. G. *Appl. Phys. A: Mater* **2006**, *82*, 615.

(17) Taberna, L.; Mitra, S.; Poizot, P.; Simon, P.; Tarascon, J. M. *Nat. Mater.* **2006**, *5*, 567.

(18) Conway, B. E. *J. Electrochem. Soc.* **1991**, *138*, 1539.

HASYLAB synchrotron facility at DESY in Hamburg. The E4 station provided a focused beam from an Au-coated toroidal mirror with a focal spot of about 5 mm × 1 mm on the sample. A Si(111) double-crystal monochromator was used with about 1 eV resolution at the Fe K-edge (7112 eV). Harmonics were effectively eliminated by a plane Au-coated mirror and by a slight detuning of the second monochromator crystal, keeping the intensity at 60% of the rocking curve with the beam stabilization feedback control. The intensity of the monochromatic X-ray beam was measured by three consecutive ionization chambers filled with argon at a pressure of 60, 300, and 600 mbar in the first, second, and the third, respectively.

Intermediate composites were prepared as self-supporting pellets with an absorption thickness ( $\mu d$ ) of about 1.5 above the Fe K-edge. The reference Fe samples with known valence state ( $\text{FeSO}_4 \cdot 7 \text{H}_2\text{O}$ ,  $\text{FePO}_4 \cdot 2 \text{H}_2\text{O}$ ,  $\alpha\text{-FeOOH}$ ,  $\text{Fe}_2(\text{SO}_4)_3 \cdot 5 \text{H}_2\text{O}$ ,  $\text{LiFePO}_4$ ) were prepared on multiple layers of adhesive tape. Stacking of layers improved the homogeneity of the samples. The number of layers was chosen to get the attenuation of  $\sim 1$  above the Fe K-edge. The samples were mounted on a sample holder in a vacuum chamber of the beamline between the first and second ionization chamber. In the XANES region equidistant energy steps of 0.5 eV were used, while for the EXAFS region equidistant  $k$ -steps ( $\Delta k \approx 0.03 \text{ \AA}^{-1}$ ) were adopted with an integration time of 1 s/step. Two repetitions were superimposed to improve the signal-to-noise ratio. In all experiments the exact energy calibration was established with simultaneous absorption measurements on a 7- $\mu\text{m}$  thick Fe metal foil placed between the second and third ionization chamber.

### 3. Results and Discussion

The initial xerogel prepared in this study contained all the reactants needed for formation of an active material ( $\text{LiFePO}_4$ ). It is essential that the iron was added in the form of citrate. On one hand, citrate serves as an efficient complexation agent in formation of a homogeneous gel. More important for the present context, however, is the fact that during heat treatment the citrate decomposes into gases such as  $\text{H}_2\text{O}$  ( $m/z = 18$ ),  $\text{CO}$  ( $m/z = 28$ ), and  $\text{CO}_2$  ( $m/z = 44$ ) (Figure 1a,b) and into a solid matter which at higher temperatures transforms into a conductive carbon film (Figure 1c).

From extensive TGA-MS measurements of samples prepared by heating the initial xerogel to different temperatures we estimate that about 83% of the citrate is transformed into gases and only about 17 wt % is deposited within the final composite as carbon film. Rough inspection of Figure 1 shows that the gases are most vigorously evolved between 200 and ca. 310 °C. In other words, it seems that the basic porosity, which later in a battery serves for fast ionic conduction, is created already at relatively low temperatures. Although the solid decomposition products are formed simultaneously, they have been shown to transform into an electronically conductive carbon phase at much higher temperatures (above ca. 500 °C).<sup>19</sup> The third functional phase, the crystalline  $\text{LiFePO}_4$  serving for storage of lithium, is formed at about 440 °C (seen as an endothermic peak in Figure 1a). The point of  $\text{LiFePO}_4$  crystallization is crucial for the final materials architecture because at that point the matter becomes much stiffer, allowing only minor morpho-

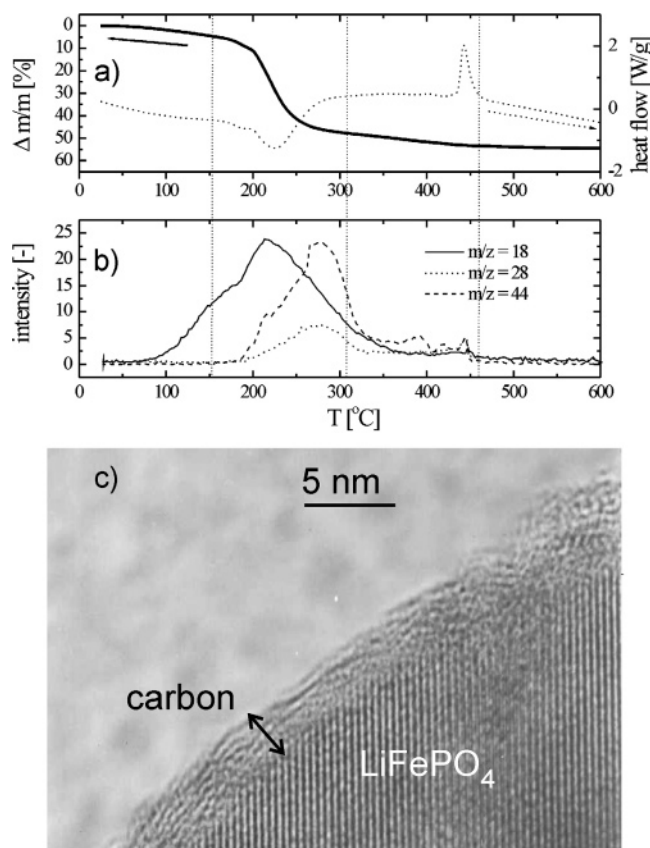


**Figure 1.** (a) Thermogravimetric analysis of LFPgel under inert atmosphere (Ar) at a heating rate of 10 °C/min coupled with (b) mass spectroscopy: solid line,  $m/z = 18$  ( $\text{H}_2\text{O}$ ); dashed line,  $m/z = 28$  ( $\text{CO}$ ); dotted line,  $m/z = 44$  ( $\text{CO}_2$ ). (c) HR-TEM image of carbon nanocoating on  $\text{LiFePO}_4$  as a product of citrate degradation at 700 °C.

logical modifications upon further heating. For this reason, we first discuss the compositional, structural, and morphological changes below and near the crystallization point of  $\text{LiFePO}_4$ , while in the second part we mainly focus on the changes occurring in the composite once  $\text{LiFePO}_4$  has already crystallized. In the end, we present in detail all the morphological and compositional aspects of the final composite that occurs at 700 °C and comment on these aspects in terms of optimized electrochemical performance.

**3.1. Compositional, Structural, and Microstructural Development Below the Crystallization Temperature of  $\text{LiFePO}_4$ .** Evolution of gases due to citrate degradation (Figure 1a) leads to a progressive formation of pores (Figure 2 a–d). At 310 °C, a significant porosity develops with typical pore sizes of ca. 30–50 nm and quite a narrow size distribution. At temperatures higher than 310 °C, evolution of gases continues, although at a much lower rate (Figure 1a). This effect, together with the process of crystallization occurring at about 440 °C, produces a denser material containing a hierarchical system of interconnected internal pores that end up in relatively large openings on the surface of individual particles (Figure 2e).

To obtain more information about the actual structural and compositional changes within the solid amorphous matrix during heating we used several techniques, among them IR-ATR (Figure 4). First, we note that in the initial xerogel (LFPgel) the portion of the spectrum from 1800 to 1200  $\text{cm}^{-1}$  is very similar to that shown by Clausén et al.,<sup>20</sup> where

(19) Moskon, J.; Dominko, R.; Gaberscek, M.; Cerc-Korosec, R.; Jamnik, J. *J. Electrochem. Soc.* **2006**, *153*, A1805.



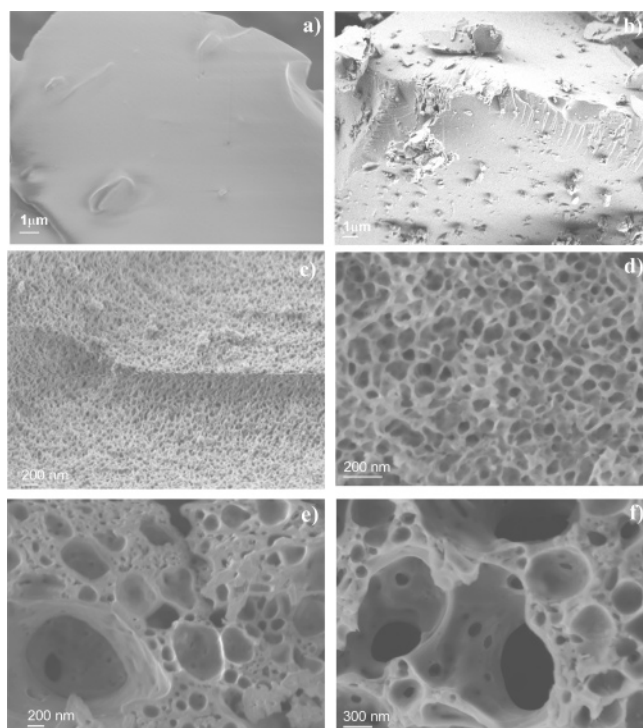


**Figure 2.** SEM micrographs for (a) LFPgel, (b) LFP155, (c) LFP200, (d) LFP310, (e) LFP465, and (f) LFP550 composites (for detailed sample descriptions see Experimental Section).

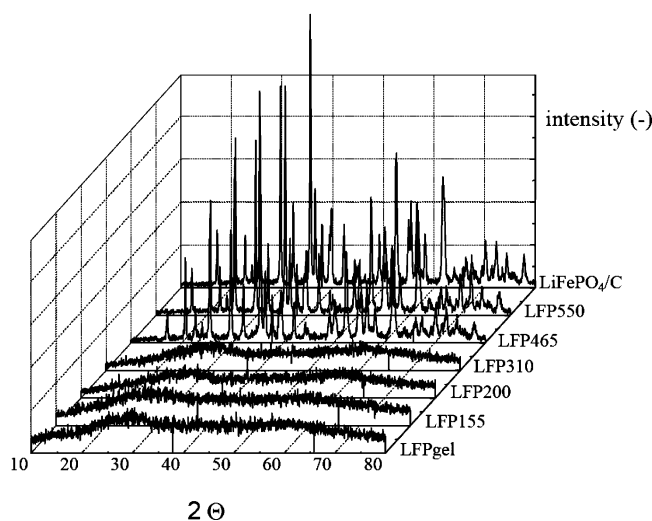


**Figure 3.** X-ray diffraction patterns for LFPgel, LFP155, LFP200, LFP310, LFP465, LFP550, and LiFePO<sub>4</sub>/C composites.

formation of an Al(III)–citrate complex was investigated. Complexation of iron with citric acid is an expected, well-documented phenomenon,<sup>21–24</sup> so we mainly focus here on the changes that occur during heat treatment of the LFPgel. It is worth mentioning that the bands (many pairs merging into a shoulder) in the middle frequency range are due to  $\nu_{\text{asym}}(\text{CO}_2^-)$  and symmetric  $\nu_{\text{sym}}(\text{CO}_2^-)$  stretching vibrations

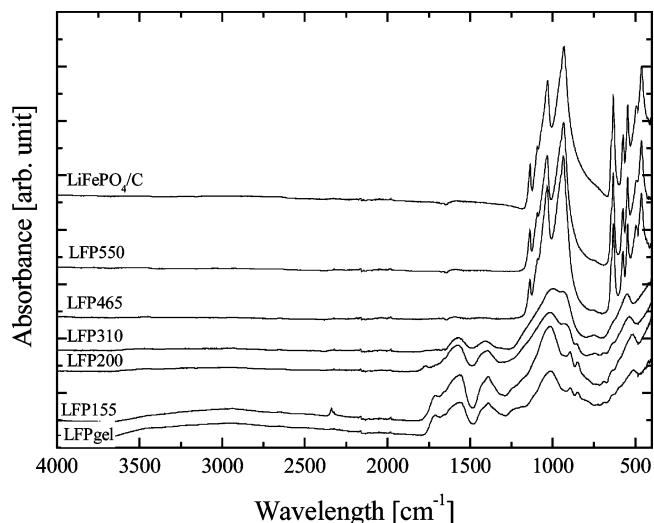


**Figure 4.** IR-ATR spectra for LFPgel, LFP155, LFP200, LFP310, LFP465, LFP550, and LiFePO<sub>4</sub>/C composites.

of the carboxylate group<sup>21,22</sup> and bands in the lower frequency region are due to the citrate anion and the PO<sub>4</sub> group. For example, the strong band at 1012 cm<sup>−1</sup> reflects the asymmetric stretching vibration, and the band at 550 cm<sup>−1</sup> represents the  $\nu_4(\text{O}–\text{P}–\text{O})$  bending vibration of the PO<sub>4</sub> group in the phosphate complex.<sup>25</sup> The broad band from 3600 to 2600 cm<sup>−1</sup> contains several typical vibrations: a band due to O–H stretching modes in coordinated water or  $\nu\text{OH}$  of carboxylic acid; an asymmetrical and a symmetrical stretching of CH<sub>2</sub> around 2900 cm<sup>−1</sup>; and intermolecular H-bridged vibrations between 2700 and 2300 cm<sup>−1</sup>. A comparison of the spectrum for LFP155 with the spectrum for LFPgel reveals only two minor changes which, however, already reflect an initial stage of gel degradation. The weaker intensity of the broad band in the range from 3600 to 2600 cm<sup>−1</sup> can be attributed to partial removal of water, which is fully consistent with the results of TGA-MS (cf. Figure 1b). Less expected, and seemingly inconsistent with TGA-MS, is the appearance of the band at 2340 cm<sup>−1</sup> (assigned to stretching of occluded CO<sub>2</sub>) and partial removal of unbounded carboxylic acids (the lower intensity of the band at 1711 cm<sup>−1</sup>). It seems that partial decomposition of the citric complex already begins below 155 °C. The resulting CO<sub>2</sub>, however, is not released into the surrounding atmosphere but supposedly remains entrapped within the bulk material. We presume that in this stage the bulk matter is relatively rigid. Further heat treatment to 200 °C leads to an even weaker broad band in the range from 3600 to 2600 cm<sup>−1</sup>, while the bands at 2340 (assigned to stretching of occluded CO<sub>2</sub>) and 1711 cm<sup>−1</sup> (unbounded carboxylic acids) completely disappear. The main difference with respect to previous spectra, however, is the appearance of the P–O symmetric stretching vibrations at 939 cm<sup>−1</sup>. These vibrations could be attributed to formation of structures containing connected PO<sub>4</sub> tetrahedra, which could represent the first organized nucleoli in the otherwise still distinctly amorphous surroundings. In parallel to this ordering, formation of bidentate bridging iron complexations has been reported in

- (20) Clausen, M.; Öhman, L. F.; Persson, P. *J. Inorg. Biochem.* **2005**, *99*, 716.  
 (21) Francis, A. J.; Dodge, C. J. *Appl. Environ. Microb.* **1993**, *59*, 109.  
 (22) Matzapetakis, M.; Raptopoulou, C. P.; Tsohos, A.; Papaefthymiou, V.; Moon, N.; Salifoglou, A. *J. Am. Chem. Soc.* **1998**, *120*, 13266.  
 (23) Gautier-Luneau, I.; Fouquard, C.; Merle, C.; Pierre, J.-L.; Luneau, D. *J. Chem. Soc., Dalton Trans.* **2001**, 2127.  
 (24) Bino, A.; Shweky, I.; Cohen, S.; Bauminger, E. R.; Lippard, S. J. *Inorg. Chem.* **1998**, *37*, 5168–5172.

- (25) Stoch, A.; Brozek, A.; Blazewicz, S.; Jaszczyński, W.; Stoch, J.; Adamczyk, A.; Roj, I. *J. Mol. Struct.* **2003**, *651*, 389.

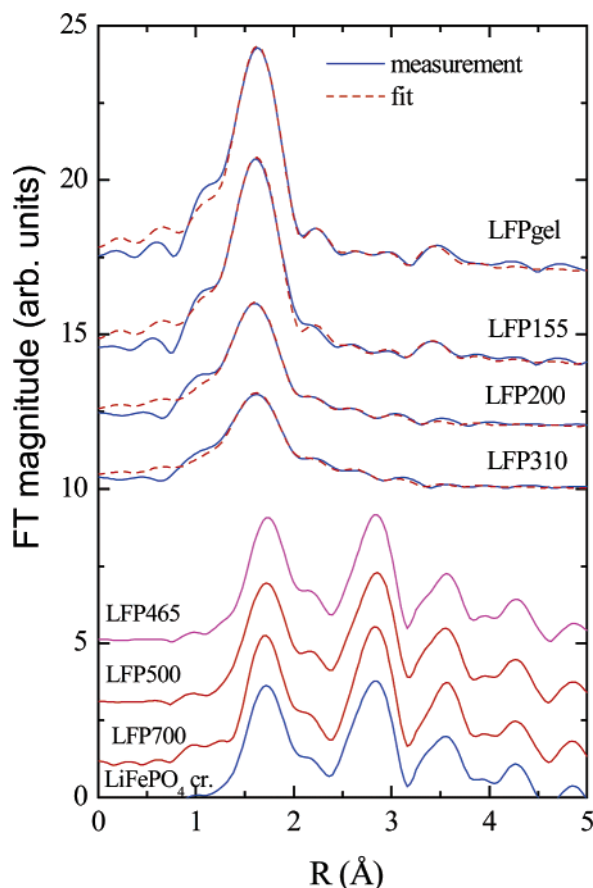


**Figure 5.**  $k^3$ -weighted Fourier transform magnitude of Fe K-edge EXAFS spectra of the LFPgel precursor, three amorphous intermediate composites LFP155, LFP200, LFP310, and three crystalline intermediate composites LFP465, LFP500, LFP700 compared with a reference crystalline  $\text{LiFePO}_4$  compound calculated in the  $k$  range from 4.7 to  $12.5 \text{ \AA}^{-1}$ : experimental data (solid line) and EXAFS model (dashed line).

the literature.<sup>26,27</sup> A new quality of organization of  $\text{PO}_4$  tetrahedra at  $200^\circ\text{C}$  is also observed later in this paper with EXAFS.

In LFP310 the asymmetric  $\nu_{\text{asym}}(\text{C}-\text{O})$  and symmetric  $\nu_{\text{sym}}(\text{C}-\text{O})$  stretching vibrations become very weak, in accordance with the large mass loss in the temperature range between 200 and  $310^\circ\text{C}$ . The other vibrational bands stemming from citric acid become negligible. The band at  $938 \text{ cm}^{-1}$  (symmetrical stretching of  $\text{PO}_4$  group) becomes stronger, suggesting formation of either a higher density or a larger average size of nuclei.

The structural changes occurring during heat treatment in the local environment around Fe were further checked using a quantitative EXAFS analysis of a Fe K-edge (Figure 5). The coordination number, distance, and Debye–Waller factor of the nearest coordination shells of neighboring atoms were obtained by comparing the measured signals with model signals in a best-fit procedure. The model signals were constructed ab initio with the FEFF6 program code<sup>28,29</sup> from the set of scattering paths of the photoelectron in a tentative

**Table 1.** Parameters of the Nearest Coordination Shells around Fe Atoms the LFPgel Precursor and Three Amorphous Intermediate Composites LFP155, LFP200, and LFP310: Average Number of Neighbor Atoms ( $N$ ), Distance ( $R$ ), and Debye–Waller Factor ( $\sigma^2$ )<sup>a</sup>

Fe neigh.	$N$	$R [\text{\AA}]$	$\sigma^2 [\text{\AA}^2]$
LFPgel			
O	6.0(4)	2.00(1)	0.006(1)
P	0.9(3)	3.19(1)	0.006(3)
P	1.2(6)	3.73(2)	0.008(4)
LFP155			
O	6.0(4)	2.00(1)	0.007(1)
P	0.7(3)	3.19(3)	0.005(3)
P	1.7(5)	3.74(3)	0.008(3)
LFP200			
O	4.5(3)	1.99(1)	0.009(1)
O	0.6(2)	2.45(1)	0.020(1)
P	0.5(2)	3.18(1)	0.004(2)
LFP310			
O	4.0(8)	1.99(1)	0.009(1)
O	1.8(2)	2.45(1)	0.020(1)
P	0.5(2)	3.20(2)	0.004(2)

<sup>a</sup> Uncertainty of the last digit is given in parentheses. A best fit is obtained with the amplitude reduction factor  $S_0^2 = 0.75$ .

spatial distribution of neighboring atoms and taking into account the elemental composition of the samples. The atomic species of neighbors in consecutive neighbor shells were recognized by their specific scattering factors and phase shifts. The model was compared with the measured spectra in the  $k$ -range from 4.7 to  $13.2 \text{ \AA}^{-1}$  using a  $k^3$ -weighted Hanning window. Best-fit structural parameters obtained in the  $R$  range from 1.2 to  $3.7 \text{ \AA}$  are collected in Table 1. The quality of fit is shown in Figure 5. The results show that in the LFPgel sample Fe atoms are coordinated to six oxygen atoms at  $1.99 \text{ \AA}$  in the first coordination shell. Phosphorus atoms are found in the second coordination shell: one at  $3.19 \text{ \AA}$  and another at  $3.73 \text{ \AA}$ . The amorphous LFP155 sample exhibits practically the same local structure around Fe atoms, i.e., no significant structural changes appear surrounding Fe during thermal decomposition up to  $155^\circ\text{C}$ . Significant changes are observed in the local structure around Fe atoms at  $200^\circ\text{C}$  (LFP200). A decrease is seen in the coordination number in the first shell with about four oxygen atoms at  $1.99 \text{ \AA}$ . The number of phosphorus atoms in the second coordination shell also decreases: on average, there are only 0.5 phosphorus atoms at the shorter distance of  $3.18 \text{ \AA}$ , and no phosphorus atoms are present at the larger distance of  $3.73 \text{ \AA}$ . An additional coordination shell is detected at  $2.45 \text{ \AA}$ , on average composed of about 0.6 oxygen atoms. The Debye–Waller factor is relatively large, indicating a large structural disorder in this coordination shell. A similar structure around Fe atoms is found in the LFP310 sample: the first coordination shell is composed of 4 oxygen atoms at  $1.99 \text{ \AA}$ , on average 0.5 phosphorus atoms are present at a distance of  $3.18 \text{ \AA}$ , and about 2 oxygen atoms are present at  $2.45 \text{ \AA}$ .

Figure 6a shows the normalized Fe XANES spectra of the seven samples and, additionally, of four reference compounds ( $\text{FeSO}_4 \cdot 7 \text{ H}_2\text{O}$ ,  $\text{FePO}_4 \cdot 2 \text{ H}_2\text{O}$ ,  $\text{Fe}_2(\text{SO}_4)_3 \cdot 5 \text{ H}_2\text{O}$ ,  $\text{LiFePO}_4$  crystal) with known Fe valence states and extracted by a standard procedure.<sup>30</sup> The zero energy is taken at the first inflection point in the corresponding metal spectrum, i.e., at the 1s ionization threshold in the corresponding metal,

(26) Francis, A. J.; Dodge, C. J. *Appl. Environ. Microb.* **1993**, *59*, 109.

(27) Nakamoto, K. *Infrared and Raman Spectra of Inorganic and Coordination Compounds*; John Wiley & Sons: New York, 1986; p 253.

(28) Rehr, J. J.; Albers, R. C.; Zabinsky, S. I. *Phys. Rev. Lett.* **1992**, *69*, 3397.

(29) Ravel, B.; Newville, M. *J. Synchrotron Radiat.* **2005**, *12*, 537.

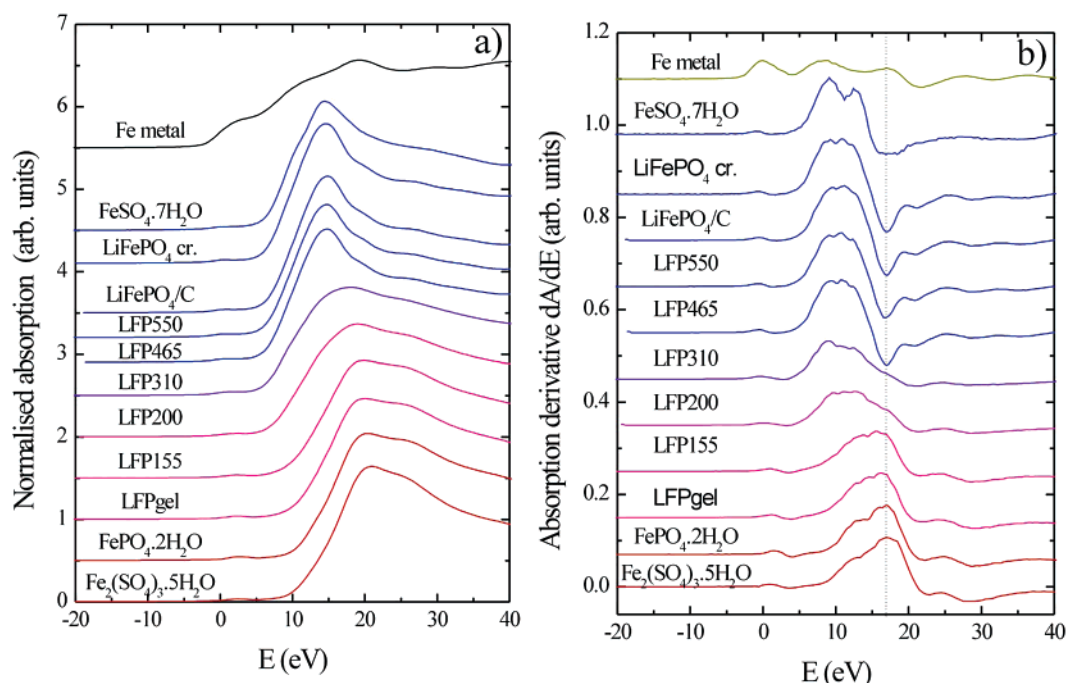


**Figure 6.** (a) Fe XANES spectra measured on LiFePO<sub>4</sub> samples taken at different stages of the sol gel synthesis and reference Fe compounds with known Fe valence states (FeSO<sub>4</sub>·7 H<sub>2</sub>O, FePO<sub>4</sub>·2H<sub>2</sub>O, Fe<sub>2</sub>(SO<sub>4</sub>)<sub>3</sub>·5H<sub>2</sub>O, LiFePO<sub>4</sub> crystal). Zero energy is taken at the Fe K-edge position in Fe metal (7112.0 eV). (b) Derivatives of the Fe XANES spectra from part a.

which marks the 1s ionization threshold in Fe metal. By convention, the K-shell contribution is obtained by removing the extrapolated preedge (−50 to −20 eV) trend and normalized to a unit K-edge jump.

The shape of the K-edge and the preedge resonances are characteristic for the local symmetry of the investigated atom.<sup>30–33</sup> The energies of the valence orbitals, and therefore the energy position of the edge and preedge features, are correlated with the valence state of the investigated atom in the sample. With increasing oxidation state, each absorption feature is shifted to higher energy. The largest shifts, up to a few electronvolts per oxidation state, are observed at the edge position defined by the inflection point.<sup>30,34–36</sup> For atoms with the same type of ligand, similar composition, and similar local symmetry, a linear relation was established between the edge shift and the valence state.<sup>30,33,34,36</sup>

From the spectra of the reference samples with known iron oxidation states (FeSO<sub>4</sub>·7 H<sub>2</sub>O, FePO<sub>4</sub>·2H<sub>2</sub>O, Fe<sub>2</sub>(SO<sub>4</sub>)<sub>3</sub>·5H<sub>2</sub>O, LiFePO<sub>4</sub> crystal) we found that the Fe K-edge shifts 4.0–4.5 eV per valence state (Figure 6a), in agreement with previous observations.<sup>37</sup> Absorption derivatives of the Fe K-edge profiles from Figure 6a are plotted in Figure 6b to

facilitate the comparison of edge shifts. The change in Fe valence state during the process of sol–gel synthesis is clearly indicated by the edge shift. The energy position of the Fe K-edge of the LFPgel coincides with the Fe K-edge position of the trivalent Fe reference compounds Fe<sup>III</sup>PO<sub>4</sub>·2H<sub>2</sub>O, Fe<sup>III</sup>(SO<sub>4</sub>)<sub>3</sub>·5H<sub>2</sub>O, which indicates that the oxidation number of all iron in the LiFePO<sub>4</sub> gel is +3. With increasing temperature, the position of the Fe K-edge shifts to lower values, indicating a partial reduction of iron. At 465 °C, almost all Fe atoms in the sample are in divalent form. The Fe K-edge coincides with that measured on the final crystalline LiFePO<sub>4</sub> product.

The changes in the local environment of iron atoms during heating were also investigated using Mössbauer spectroscopy. All samples were measured in the transmission mode (shown in Figure 7). Sample LFP465 was also measured in emission with conversion electrons. Conversion electrons can escape from depths as low as 300 nm and make contributions to Mössbauer spectra that are more surface sensitive than the transmission spectra, which are sensitive to the bulk material. The LFPgel precursor spectrum only shows a contribution due to Fe<sup>III</sup> and could be fitted with two quadrupole doublets. Sample LFP155 already shows 8 atom % of Fe<sup>II</sup>, while the rest of the spectrum resembles the features of the LFP gel. The LFP200 sample shows a more distorted Fe<sup>III</sup> environment compared to the LFPgel, and the contribution of the Fe<sup>II</sup> species can be described with two relatively broad quadrupole doublets. In the LFP310 sample the contribution of the Fe<sup>II</sup> species further increases with hyperfine parameters similar to LFP200.

Summarizing the above results, we propose the tentative structure of the initial xerogel as shown in Figure 8. In this conception each ferric iron (as suggested by EXAFS, XANES, IR-ATR, and Mössbauer spectroscopy) is supposed

- (30) Wong, J.; Lytle, F. W.; Messmer, R. P.; Maylotte, D. H. *Phys. Rev. B* **1984**, *30*, 5596.
- (31) Kau, L. S.; Spira-Solomon, D. J.; Penner-Hahn, J. E.; Hodgson, K. O.; Solomon, E. I. *J. Am. Chem. Soc.* **1987**, *109*, 6433.
- (32) Lytle, F. W.; Greigor, R. B.; Panson, A. *J. Phys. Rev. B* **1988**, *37*, 1550.
- (33) Arčon, I.; Mirtić, B.; Kodre, A. *J. Am. Ceram. Soc.* **1998**, *81*, 222.
- (34) Bajt, S.; Sutton, S. R.; Delaney, J. S. *Geochim. Cosmochim. Acta* **1994**, *58*, 5209.
- (35) Kemner, K. M.; et al. *J. Synchrotron Radiat.* **2001**, *8*, 949.
- (36) Ressler, T.; Brock, S. L.; Wong, J.; Suib, S. L. *J. Synchrotron Radiat.* **1999**, *6*, 728.
- (37) Benfatto, M.; Solera, J. A.; Ruiz, J. G.; Chaboy, J. *Chem. Phys.* **2002**, *282*, 441.
- (38) Fujii, H.; Hokabe, T.; Kamigaichi, T.; Okamoto, T. *J. Phys. Soc. Jpn.* **1977**, *43*, 41.



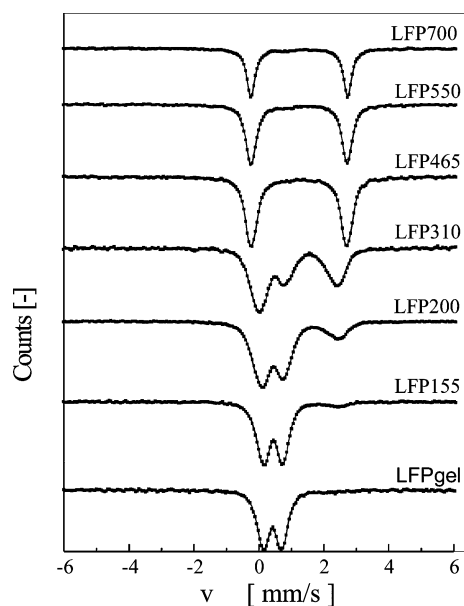


**Figure 7.** Mössbauer spectra of composite samples prepared at different temperatures.

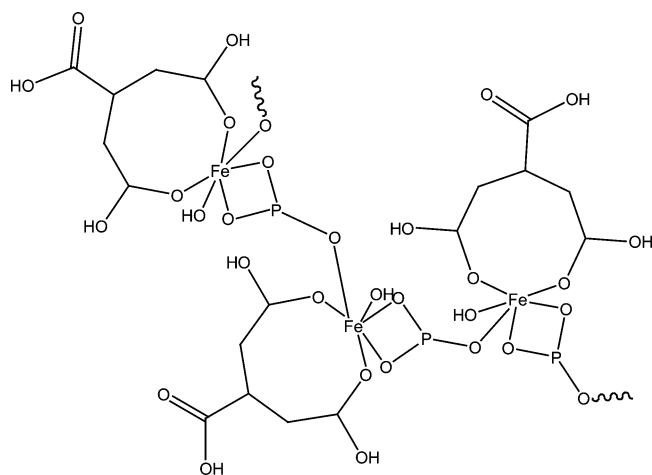


**Figure 8.** Proposed structure of the LFPgel.

to be connected to a citrate anion and two phosphate anions (for clarity, hydrogen bonds are not shown). Upon thermal treatment, different intermediate structures are formed with a tendency to form nuclei as consistently detected by three independent techniques: IR-ATR spectroscopy suggested ordering of  $\text{PO}_4$  groups, while both EXAFS/XANES and Mössbauer spectroscopy showed arranged domains with an environment similar to that in crystalline material.

The continuous structural changes that occur during heating below the crystallization point of  $\text{LiFePO}_4$  suggest a significant textural flexibility which is a precondition for formation of porous architectures as shown in Figure 2. As citrate is completely homogeneously distributed in the initial xerogel, it is clear that the evolving gases create an interconnected 3-D web of pores throughout the material. This feature was confirmed by observing a number of material cross-sections under SEM (not shown). Additionally, development of porosity with temperature was followed by measuring  $\text{N}_2$  adsorption isotherms on all samples prepared in this study (see Experimental Section). The results gathered in Figure 9a,b show that after heating above 200 °C but

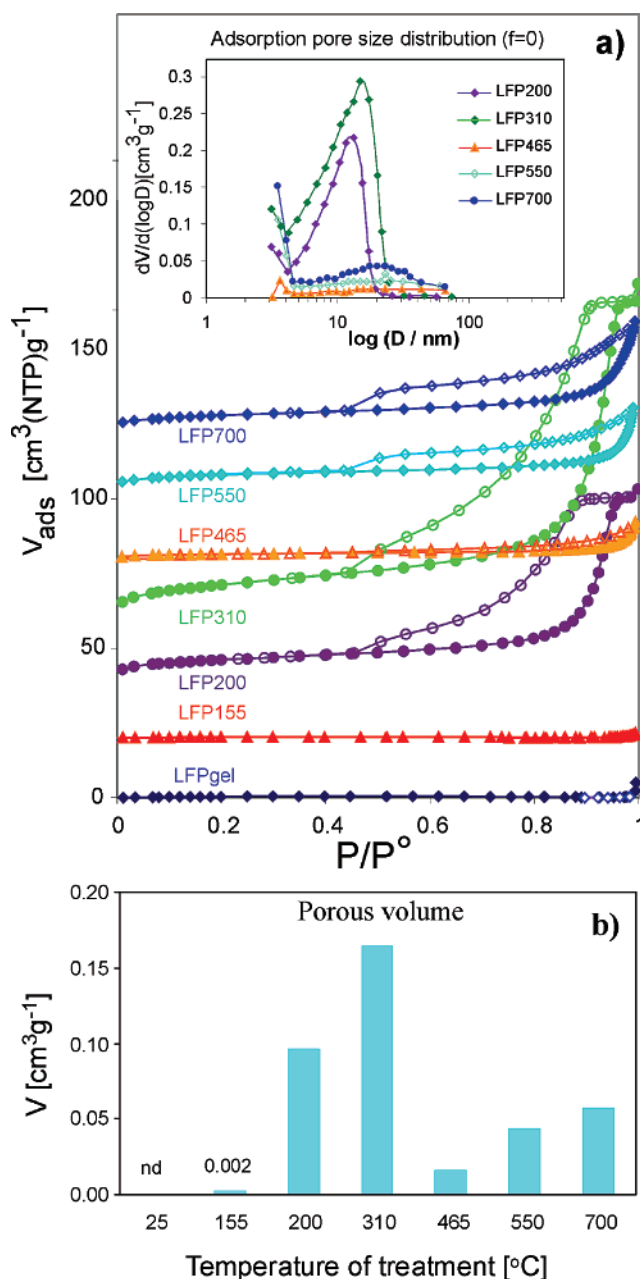


**Figure 9.** (a)  $\text{N}_2$  adsorption isotherms of  $\text{LiFePO}_4/\text{C}$  composites prepared at different temperatures. The filled symbols correspond to the adsorption branch and the empty symbols to the desorption branch. For the sake of readability, the isotherms are shifted upward by  $n \times 100 \text{ mL g}^{-1}$ . (Inset) BJH distribution of pores from the desorption branch. (b) Development of pore volume over the sample treatment temperature.

below the crystallization temperature (440 °C) the samples exhibit significant mesoporosity with a relatively narrow distribution of pore sizes, in good agreement with SEM observations (Figure 2c,d).

Above the crystallization point the pore volume significantly decreases, the width of pores increases, and the distribution of sizes becomes much wider. It seems that the process of crystallization involves significant spatial rearrangement of matter which results in material densification while preserving a substantial amount of pores. In fact, from the point of view of battery performance, partial densification is a desirable effect since it improves the energy density. It is crucial, however, that most of the pores remain interconnected. Closer inspection of the morphology just above the



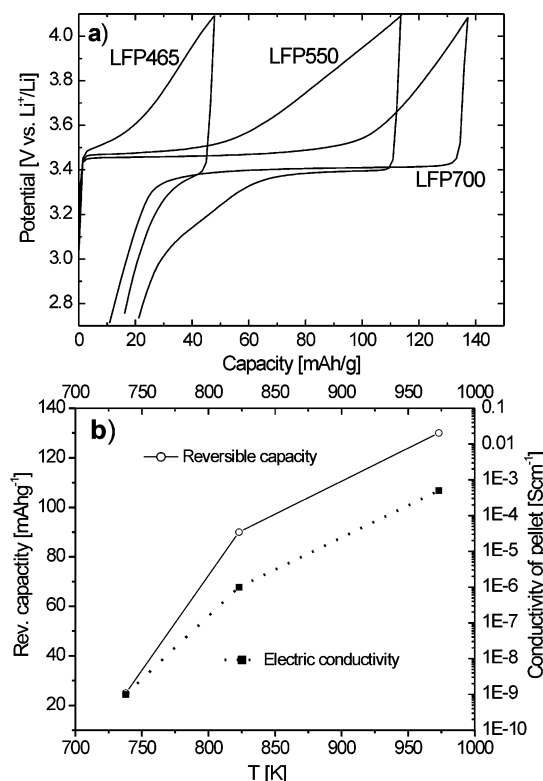


**Figure 10.** (a) Charge–discharge curves of LiFePO<sub>4</sub>/C samples treated at different temperatures (indicated within the labels). In all cases, the current was set to  $C/2$  (ca. 85 mA/g). (b) Development of reversible capacity and electric conductivity with temperature of sample treatment.

crystallization point of LiFePO<sub>4</sub> (Figure 2e) shows that within the basic fine porous web larger pores are also created. Evolution of the adsorption branch into a nearby nonporous type II isotherm is a clear indication of these large pores. Their occurrence can be correlated with a spike in the CO<sub>2</sub> curve at the point of LiFePO<sub>4</sub> crystallization (Figure 1a). This spike is probably caused by the released crystallization energy (Figure 1a), which helps degrade the last amount of carboxyl groups.

In summary, the present results clearly demonstrate that the hierarchical nature of the mesoporous–macroporous web is due to the changing rate of gas evolution in the temperature range where the material is still soft enough to allow considerable morphological changes. This mechanism can now explain several previous observations. For example, in ref 10 we found that the heating rate during preparation of LiFePO<sub>4</sub>/carbon composites affected the distribution of pore sizes in the final material, which in turn influenced the performance of LiFePO<sub>4</sub> composites. Looking back, we can now see that the samples with wider pore distributions, indicating a more developed hierarchy of ionic pathways, had a better performance than those with narrower size distributions. Moreover, the very fact that the pore distribution affected the electrode performance confirms the importance of ionically conducting networks, a feature neglected in most studies until now.

**3.2. Materials Development Above the Crystallization Temperature of LiFePO<sub>4</sub>.** Above 440 °C (the crystallization point of LiFePO<sub>4</sub>) the basic material morphology remains practically frozen in position and no dramatic changes can be observed up to 700 °C (cf. Figure 2e,f).

**Table 2. Comparison of Average Valence State Determined with Mössbauer Spectroscopy and XANES**

sample	Mössbauer spectroscopy			XANES	
	CS [mm/s]	QS [mm/s]	av. Fe valence	$\Delta E$ (eV)	av. Fe valence
LFPgel	0.416	0.569	+3.0	16.4	+3.0(1)
LFP155	1.14	2.585	+2.92	16.2	+2.9(1)
LFP200	0.428	0.603	+2.72	15.0	+2.6(1)
LFP310	1.328	0.771	+2.40	14.3	+2.4(1)
LFP465	0.376		+2.05	13.0	+2.1(1)
LFP550	0.468	0.71	+2.04	12.9	+2.0(1)
LiFePO <sub>4</sub> /C	1.217	0.388	+2.04	12.9	+2.0(1)
reference compounds	1.2231	0.485	+2.0		
FePO <sub>4</sub> ·2H <sub>2</sub> O			+3.0	16.6	+3
LiFePO <sub>4</sub> cryst. <sup>30</sup>			+2.0	12.9	+2

X-ray diffractograms (Figure 3) as well as EXAFS (Figure 5) show that at 465 °C LiFePO<sub>4</sub> is already completely crystalline and no further changes occur at higher temperatures. Also, no changes above 465 °C are seen by IR-ATR (Figure 4). However, galvanostatic testing of the material above 440 °C (Figure 10) shows significant development of the electrochemical performance with increasing temperature. The full capacity is only obtained when the temperature reaches 700 °C. To understand the reasons for the remarkable increase in capacity despite the small morphological and structural changes, we performed a range of further analyses. The possible influence of each of the three constituting phases was separately examined: the LiFePO<sub>4</sub> active material, the pores, and the carbon film.

In regard to the quality of LiFePO<sub>4</sub> itself, one could assume that at lower temperatures, although it is already crystalline, it still contains a significant amount of impurities in the form of Fe(III) compounds, which are perhaps only gradually transformed into Fe(II) at higher temperatures. Mössbauer spectroscopy and a XANES analysis, however, do not support this assumption. On the contrary, they consistently show that basically pure Fe(II) compound is already present immediately after crystallization at 465 °C (Table 2).

As mentioned above, the basic material morphology is preserved from 465 to 700 °C. N<sub>2</sub> sorption experiments (Figure 9), however, reveal significant changes in the amount of micropores (pores with a width below 2 nm). The occurrence of cracks in the carbon coating has also been observed (not shown). Finally, SEM micrographs reveal somewhat larger surface apertures at the highest temperatures (compare Figures 2e,f). All three phenomena combined could significantly increase the permeability of the electrolyte phase in the porous system and thus facilitate its access to the active inorganic phase (LiFePO<sub>4</sub>). To observe the impact of material porosity on electrochemistry in a clearer way, two series of materials were prepared with distinctly different pore sizes and distributions (Figure 11). This was done by simply selecting different heating rates during preparation of the materials. Most importantly, both heatings were carried out to exactly 700 °C, thus ensuring similar properties of the carbon nanofilm.<sup>19</sup> In this way, the effect of porosity (ionic conductivity) could be observed separately from the possible effect of the carbon film (electronic conductivity). N<sub>2</sub>

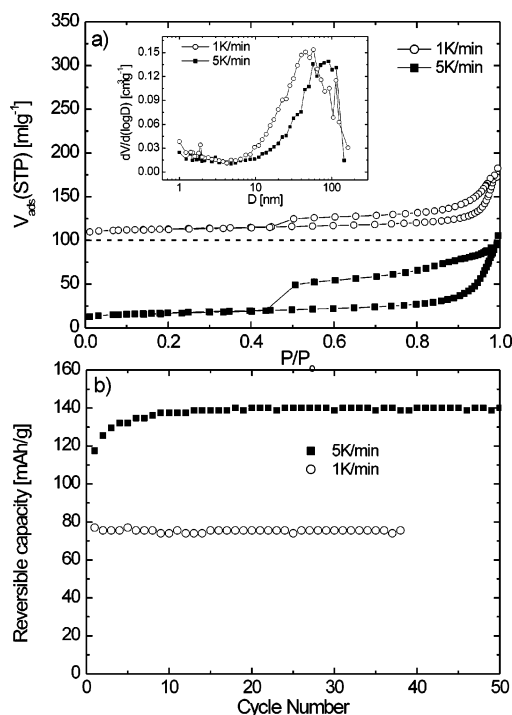


**Figure 11.** (a)  $N_2$  adsorption isotherms for two  $LiFePO_4/C$  composites prepared using different heating rates: 1 (circles) and 5K/min (squares). For the sake of readability, the isotherms are shifted upward by 100 mL g<sup>-1</sup>. (Inset) BJH distribution of pores from the adsorption branch. (b) Reversible capacity as a function of cycle number for both composites. The measurements were performed at a constant current of  $C/2$  (ca. 85 mA/g).

adsorption isotherms reveal that both heating rates, 1 and 5 K min<sup>-1</sup>, produced a similar micropore volume (about 0.015 mL g<sup>-1</sup> if assuming 3 wt % of carbon within the as-prepared composite). However, the composite obtained at the faster heating rate had more open and wider mesopores with an average size of 90 nm, as opposed to ca. 60 nm obtained with the slower heating rate. Similarly, the faster heating rate produced larger surface apertures (see Supporting Information). Finally, the electrochemical performance of the material with the larger and more open pores/apertures is clearly superior (Figure 11b). This result demonstrates the importance of sufficient porosity in achieving high electrochemical performance and can at least partly explain the progressive improvement of electrochemistry shown in Figure 10.

The other parameter that may play an essential role in improving the electrochemistry at higher temperatures (Figure 10) is the carbon phase, which is supposed to supply the active material with electrons. The functionality of the carbon phase, in terms of both interconnectivity and conductivity, can be elegantly tested by simply measuring the electrical conductivity of the prepared composites.<sup>19</sup> This is possible because the conductivity of the  $LiFePO_4$  phase itself is extremely low ( $<10^{-9}$  S cm<sup>-1</sup>),<sup>30</sup> so only the contribution of the carbon phase is effectively detected.

Here, it is assumed that the carbon is sufficiently conductive (the expected conductivity is above 1 S cm<sup>-1</sup>)<sup>19</sup> and forms a percolated network within the composite,<sup>19</sup> thus satisfying the basic properties required in a battery electrode. Figure 10b shows that the average conductivity of prepared composites increases significantly from 465 to 700 °C. The

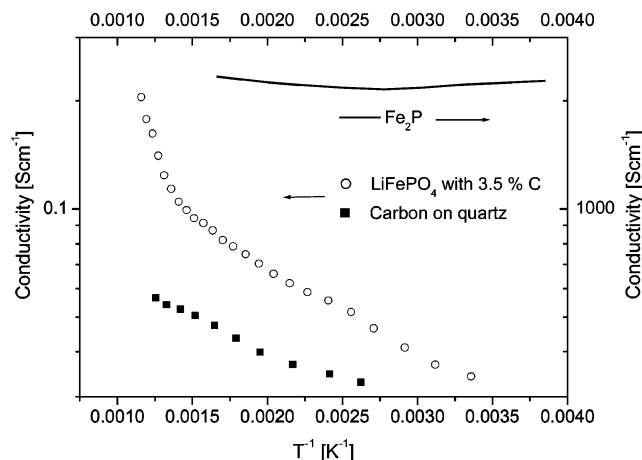


**Figure 12.** Temperature dependence of conductivity for three samples. The curves for the  $LiFePO_4/C$  composite and the carbon film on flat quartz were recorded in the frame of the present study. The curve for  $Fe_2P$  is replotted from ref 38. Both the activation energy and the conductivity range of the latter are remarkably different than the corresponding values for the former two samples.

result is fully consistent with our previous investigation of conductive carbon phases on titanates,<sup>19</sup> where heating up to 700 °C was also needed to convert citrate into a fully conductive carbon material. We might, therefore, conclude that the improvement of electrochemical performance in Figure 10a could be significantly affected not only by the development of porosity but also by the improved conductivity of the carbon phase. In order to precisely quantify such combined effects, however, extensive further kinetic studies are required.

On the basis of the results of other researchers, there is at least one further source that can influence the electrochemical performance. For example, Herle et al. have shown that in certain  $LiFePO_4$ -based materials phosphide impurities may exist<sup>8</sup> which also possess excellent electronic conductivity. Identification of the phase that is responsible for conduction in a given system is sometimes possible by measuring the activation energies for conduction in that system. Figure 12 shows the temperature dependence of conductivity for pure  $Fe_2P$ , carbon film on a quartz substrate, and the present composite material. Evidently, this sample has an activation energy similar to the carbon film on quartz but much different from that found for  $Fe_2P$ . This strongly supports the assumption that the carbon phase is responsible for conductivity in this composite material.

**3.3. Composition and Morphology of the Final Composite at 700 °C and Their Impact on Electrochemical Performance.** The material properties at 700 °C were studied in some detail in our previous work.<sup>9,10</sup> Here, we repeat the most important conclusions and complete the picture with some important new results. At 700 °C the as-prepared powder consists of particles with typical dimensions of 0.5–20  $\mu$ m.<sup>9,10,39</sup> Each individual particle has a single-crystalline electron diffraction pattern due to  $LiFePO_4$ <sup>39</sup> but also exhibits a significant porosity. The pores have a very wide size distribution, ranging from 1 to 200 nm (as detected using  $N_2$  adsorption, see Figure 9) with an average value of about

(39) Gaberscek, M.; Dominko, R.; Bele, M.; Remskar, M.; Hanzel, D.; Jamnik, J. *Solid State Ion* **2005**, 176, 1801.

50 nm. The meso- and micropores occupy about 10 vol % of the total particle volume.<sup>10</sup> Additionally, numerous larger apertures (such as those seen in Figure 2e,f) are observable by optical methods on the particle surfaces. The combination of electrical and electrochemical methods gives clear evidence that a percolating network of conductive carbon exists within these porous LiFePO<sub>4</sub> particles. The exact carbon morphology could only be determined on the particle surface, where an about 1–2 nm thick, uniform film was detected.<sup>9</sup> Using other substrates such as TiO<sub>2</sub> and quartz<sup>19</sup> we found that citrate also forms such surface films when it is present in sufficient quantities. Given the mechanism of material formation proposed in this paper, it seems reasonable to assume that such a carbon film (1–2 nm thick) is also deposited on the surface of most, if not all, pores. As the pores are interconnected, so is the carbon film. The assumption of such a continuous carbon film on all material surfaces can be checked by a simple calculation if we know that the material's specific surface area is about 25 m<sup>2</sup>/g and the total amount of carbon is 3.5 wt %. Assuming further that the true carbon density is about 2 g/cm<sup>3</sup>, one finds a film thickness value of ca. 0.9 nm, a surprisingly good agreement with the actually observed film thickness on the outer particle surface (1–2 nm). Such a thin film on the wall of a typical pore with a diameter of 50 nm represents basically no obstruction for the flow of electrolyte through the pore. Similarly, the carbon film is thin enough that Li ions can pass from the electrolyte through the film into the solid LiFePO<sub>4</sub>, where they are stored. It is, of course, the same carbon which simultaneously provides electrons near the spots of Li ion insertion, thus satisfying the material's electroneutrality. This parallel supply of ions and electrons to a large specific surface area makes this material useful at very high *C* rates.<sup>9,39</sup> On the other hand, as the porous pathways are hierarchically structured, they occupy a relatively small fraction of the total volume, which is reflected in the high tap density of this material, about 1.9 g/cm<sup>3</sup>. In this way, the material represents a good compromise between a high rate and high density. Now, as the preparation route leading to such a materials architecture is known, it will be interesting to use this route on other emerging materials with high inherent energy densities but extreme kinetic problems, such as borates (LiMBO<sub>3</sub>, M = Fe, Co, Mn)<sup>40</sup> and silicates (Li<sub>2</sub>MSiO<sub>4</sub>, M = Fe, Mn).<sup>11,12</sup>

(40) Legagneur, V.; An, Y.; Mosbah, A.; Portal, R.; Le Gal La Salle, A.; Verbaere, A.; Guyomard, D.; Piffard, Y. *Solid State Ion* **2001**, 139, 37.

#### 4. Conclusions

A possible strategy that can lead to the maximization of power density while preserving the inherently high energy density of advanced battery materials is the preparation of intertwined 3-D networks of ionic and electronic conductors within a given active material. This paper demonstrated the preparation of interconnected pores (i.e., ionic conductor filled with electrolyte) that are decorated with conductive carbon (electronic conductor) within micrometer-sized LiFePO<sub>4</sub> single crystals. The crucial step in this procedure is the use of citrate in the preparation of the starting gel. In the present context, this anion can be viewed as a template substance controlling the material's structure throughout the course of synthesis. Creation of hierarchically organized pores results from the stochastic and quite vigorous evolution of gases during the heat treatment of the initial gel containing citrate. Simultaneous with the evolution of gases (from ca. 200 to 440 °C), deposition of solid carbon on the walls of emerging pores takes place. During further heat treatment (up to 700 °C) the resulting thin carbon film (ca. 1–2 nm thick) is transformed into a conductive percolated carbon network serving for fast electron conduction. It seems that such a materials architecture can be achieved when the solidification/crystallization of active material occurs just above the temperature interval of vigorous degradation of organic precursor into gases and solids. In this way, the pores can remain essentially interconnected even if solidification/crystallization causes a major structural displacement, as indicated in the present case of LiFePO<sub>4</sub>.

**Acknowledgment.** This work was supported by the Slovenian Research Agency, the bilateral project BI-DE/03-04-004 of the Internationales Buero des BMBF, and the EC Research Infrastructure Action under the FP6 "Structuring the European Research Area" Programme (through the Integrated Infrastructure Initiative "Integrating Activity on Synchrotron and Free Electron Laser Science"). Access to the synchrotron radiation facility of HASYLAB (beamline E4, project II-01-44) is acknowledged, and we would like to thank K. Klementiev of HASYLAB station E4 for expert advice on beamline operation.

**Supporting Information Available:** Scanning electron micrographs of composite material prepared at different heating rates. This material is available free of charge via the Internet at <http://pubs.acs.org>.

CM062843G